Characterization, Monitoring, and Mitigation of the I/Q Imbalance in Standard C-Band Transceivers in Multi-Band Systems

Gabriele Di Rosa, *Graduate Student Member, IEEE*, Robert Emmerich,
Matheus Sena, *Graduate Student Member, IEEE*, Johannes K. Fischer, *Senior Member, IEEE*,
Colja Schubert, Ronald Freund, and André Richter, *Senior Member, IEEE*

***Abstract*—Next-generation optical communication networks aim to vastly increase capacity by exploiting a larger optical transmission window covering the S-C-L-band. Simultaneously, the clear market trend is to maximize capacity per wavelength to reduce operational costs. This approach requires an increase in spectral efficiency, resulting in stringent requirements on the transceivers, which may not be satisfied in a multi-band (MB) scenario by current commercial components designed for operation in C-band. Transceiver specifications for MB operation can be relaxed through additional digital signal processing (DSP), at the cost of additional complexity, and by more resource-intensive calibration procedures. In this context, we experimentally characterize the wavelength-dependent frequency-resolved in-phase/quadrature (I/Q) imbalance of a standard C-band IQ-modulator and coherent receiver operating in an S-C-L-band system utilizing receiver-side DSP. This operation allows us to understand the nature of the wavelength-dependency of I/Q imbalance in MB systems. In the considered scenario, we validate the effectiveness of a cost-effective strategy for transceiver impairments mitigation and monitoring based on standard wavelength-independent calibration and reduced-complexity DSP.**

***Index Terms*—Optical fiber communication, wideband networks, ultra wideband transmission, S-C-L-band, IQ imbalance, digital signal processors.**

I. INTRODUCTION

THE continuous rise in IP traffic encourages operators to accelerate the deployment of multi-band (MB) wavelength division multiplexing (WDM) systems. This solution presents itself as an advantageous short- to mid-term option for network capacity upgrade from a techno-economic perspective thanks to the efficient reuse of the existing fiber infrastructure [1]. At the same time, the required continuous reduction of cost-per-bit directs the market towards the development of transponders that maximize the data rate per wavelength [2]. This approach reduces operational costs and is particularly beneficial in MB networks, where provisioning and managing a much higher number of wavelengths are required. Moreover, if reliable transmission of high-order quadrature amplitude modulation (QAM) formats is available in the whole MB transmission window, it is possible to exploit constellation shaping to achieve fine rate-adaptivity. In turn, this allows maximizing the fiber channel capacity over the wavelength-dependent end-to-end channel, as it has been shown in recent record experiments [3]. On the other side, this approach poses stringent requirements for transceivers. While commercial solutions for C-L-band systems are available, the same is not true for the S-band, and, currently, the only logical choice for the short-term deployment of S-C-L-band networks is to employ standard C-band transceivers over the whole wavelength range. In this context, it is essential to understand the wavelength-dependency of the I/Q imbalance of C-band transceivers working outside their manufacturing range [4] and, more importantly, to assess possible compensation schemes and resulting performance penalties.

With currently available off-the-shelf components and doped fiber amplifiers, an S-C-L-band setup spanning from 1460 nm to 1608.8 nm (≈ 150 nm) has been demonstrated for dual-polarization (DP) 64 GBd 32/64-QAM with calibration and digital pre-distortion (DPD) performed through system identification at a single wavelength [5]. In this configuration, we performed the characterization of the wavelength-dependency of the I/Q imbalance considering a flat frequency response inside the signal bandwidth for the impairments [4].

In this paper, we extend the work in [4] by identifying the variation of the frequency-resolved I/Q imbalance inside the signal electrical bandwidth versus wavelength for off-the-shelf C-band transceivers working in S-C-L-band systems. We monitor the transmitter (Tx) and receiver (Rx) I/Q amplitude and phase imbalance, and I/Q skew up to half the Nyquist frequency through

---

Manuscript received November 25, 2021; revised February 1, 2022; accepted February 23, 2022. Date of publication February 28, 2022; date of current version June 1, 2022. This work was supported in part by the EU Horizon 2020 research and innovation program through the H2020-MSCA-ITN-2018 under Grant 814276 (WON), and in part by the German Ministry of Education and Research through the OptiCON under Grants 16KIS0993 and 16KIS0990. *(Corresponding author: Gabriele Di Rosa.)*

Gabriele Di Rosa and André Richter are with the VPIphotonics GmbH, 10587 Berlin, Germany (e-mail: gabriele.di.rosa@vpiphotonics.com; andre.richter@vpiphotonics.com).

Robert Emmerich, Matheus Sena, Johannes K. Fischer, Colja Schubert, and Ronald Freund are with the Fraunhofer Institute for Telecommunications Heinrich-Hertz-Institute, 10587 Berlin, Germany (e-mail: robert.emmerich@hhi.fraunhofer.de; matheus.sena@hhi.fraunhofer.de; johannes.fischer@hhi.fraunhofer.de; Schubert@hhi.fraunhofer.de; Ronald.Freund@hhi.fraunhofer.de).

Color versions of one or more figures in this article are available at https://doi.org/10.1109/JLT.2022.3154888.

Digital Object Identifier 10.1109/JLT.2022.3154888

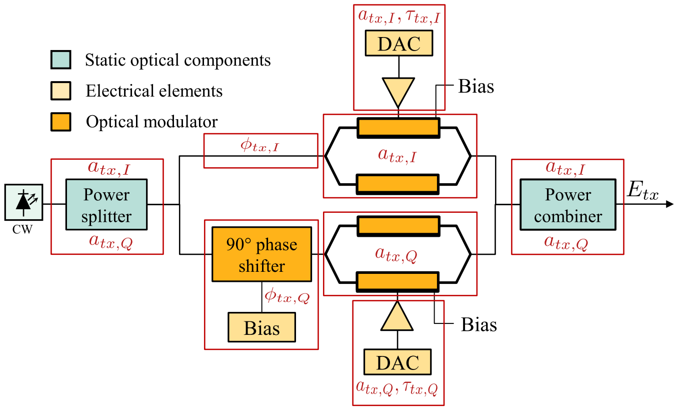

Fig. 1. Transmitter model. DAC: Digital to analog converter, CW: Continuous wave.

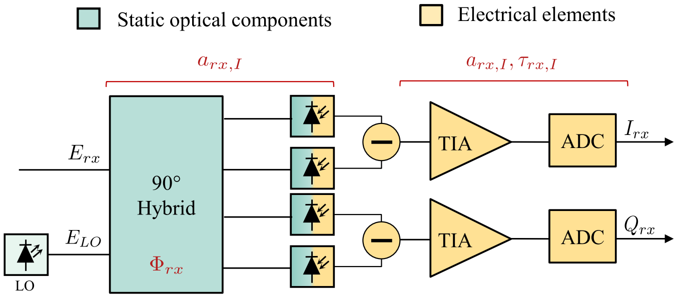

Fig. 2. Receiver model. LO: Local oscillator, TIA: Transimpedance amplifier, ADC: Analog to digital converter.

two real-valued multi-input-multi-output (MIMO) 4×4 equalizers [6]. We observe a wavelength-dependent frequency-flat I/Q imbalance when performing this operation, while the frequency-selective component remains unchanged. This observation demonstrates the feasibility of cost-effective monitoring and compensating for the wavelength-dependency of transceiver impairments in multi-band networks. Only a single calibration and standard low-complexity DSP that includes signal orthonormalization and single-tap real-valued adaptive filtering for post-equalization are necessary.

The rest of the paper is organized as follows: In Section II, we detail the model for the transceiver imbalance, focusing on the sources of I/Q imbalance. In Section III, the experimental setup used for the characterization of the transceivers is detailed. In Section IV, we describe the imbalance characterization method, and we present the experimental results. Finally, section V provides the conclusions of this work.

II. TRANSCEIVER IMBALANCE MODEL

A. Transmitter

At the transmitter side, we can write for each of the two polarization states the ideal optical output signal as:

$$\widetilde{E}_{tx}(t) = \Re\left[\left(\widetilde{I}(t) + j\widetilde{Q}(t)\right)\exp\left(j\omega_s t\right)\right], \qquad (1)$$

where $\widetilde{I}$ and $\widetilde{Q}$ are the ideal baseband in-phase and quadrature signals, ω_s is the angular oscillation frequency of the transmitter laser, and $\Re(\cdot)$ denotes the real part of a complex quantity. However, in real devices, the I and Q branches are not perfectly balanced and synchronized. The result of these imperfections is the introduction of I/Q imbalance. In Fig. 1, the general model of a single-polarization optical transmitter is shown and the sources of the different non-idealities are highlighted. For the baseband signal $u_{tx}(t) = I(t) + jQ(t)$, where $I(t)$ and $Q(t)$ are respectively the real and imaginary part, we can write in general [6]:

$$\begin{aligned} u_{tx}(t) = {} & a_{tx,I}\exp\left[j\phi_{tx,I}\right]\widetilde{I}(t+\tau_{tx,I}) + \\ & + j a_{tx,Q}\exp\left[j\phi_{tx,Q}\right]\widetilde{Q}(t+\tau_{tx,Q}), \end{aligned} \qquad (2)$$

and we can define the I/Q amplitude imbalance $\gamma_{tx} = a_{tx,Q}/a_{tx,I}$, phase imbalance $\Phi_{tx} = \phi_{tx,Q} - \phi_{tx,I}$ and I/Q skew $\Delta\tau_{tx} = \tau_{tx,Q} - \tau_{tx,I}$.

In standard C-band systems, the optical components operate in their designed wavelength range, and imperfections in the I/Q modulator's electrical elements are the dominant source of I/Q imbalance. On the contrary, the contribution of the optical components can become dominant in MB systems. In particular, the splitting ratio of the power splitter and combiner may present wavelength-dependency, introducing additional amplitude imbalance and limiting the achievable performance [7]. These components are crucial since, unlike the Mach-Zehnder modulator (MZM) and the phase shifter, they have no inherent electrical control mechanism. In principle, we can partially mitigate the wavelength-dependency of the splitting ratio through separate optimization of the digital pre-distortion (DPD) for each wavelength. This can be achieved through a per-wavelength characterization and also employing adaptive DPD approaches [8]. However, the operation comes at the cost of higher computational complexity and measurement effort.

B. Receiver

Similarly as for the transmitter, at the receiver side we find I/Q amplitude imbalance $\gamma_{rx} = a_{rx,Q}/a_{rx,I}$, phase imbalance Φ_{rx} and I/Q skew $\Delta\tau_{rx} = \tau_{rx,Q} - \tau_{rx,I}$. In Fig. 2 the single polarization receiver model is reported and, as done for the transmitter, the different sources of imbalance are specified. The electrical elements introduce skew and contribute to the creation of amplitude imbalance. At the same time, imperfections in the optical components introduce phase imbalance in the 90°-hybrid and amplitude imbalance in both, the 90°-hybrid and the balanced photodetectors. Optical hybrids, in particular, can present large deviations from the ideal performance when operating far from the design wavelength [4], [9].

Considering the imbalance just discussed, and assuming for simplicity polarization alignment between the signal and LO, we can write for the resulting differential IQ signals at the output [6]:

$$\begin{aligned} I_{rx}(t) & \propto a_{rx,I}\left[I(t)\cos\left(\Delta\omega t\right) - Q(t)\sin\left(\Delta\omega t\right)\right] \\ Q_{rx}(t) & \propto a_{rx,Q}\left[I(t)\sin\left(\Delta\omega t + \Phi_{rx}\right) + \right. \\ & \left. + Q(t)\cos\left(\Delta\omega t + \Phi_{rx}\right)\right] * \delta(t - \Delta\tau_{rx}), \end{aligned} \qquad (3)$$

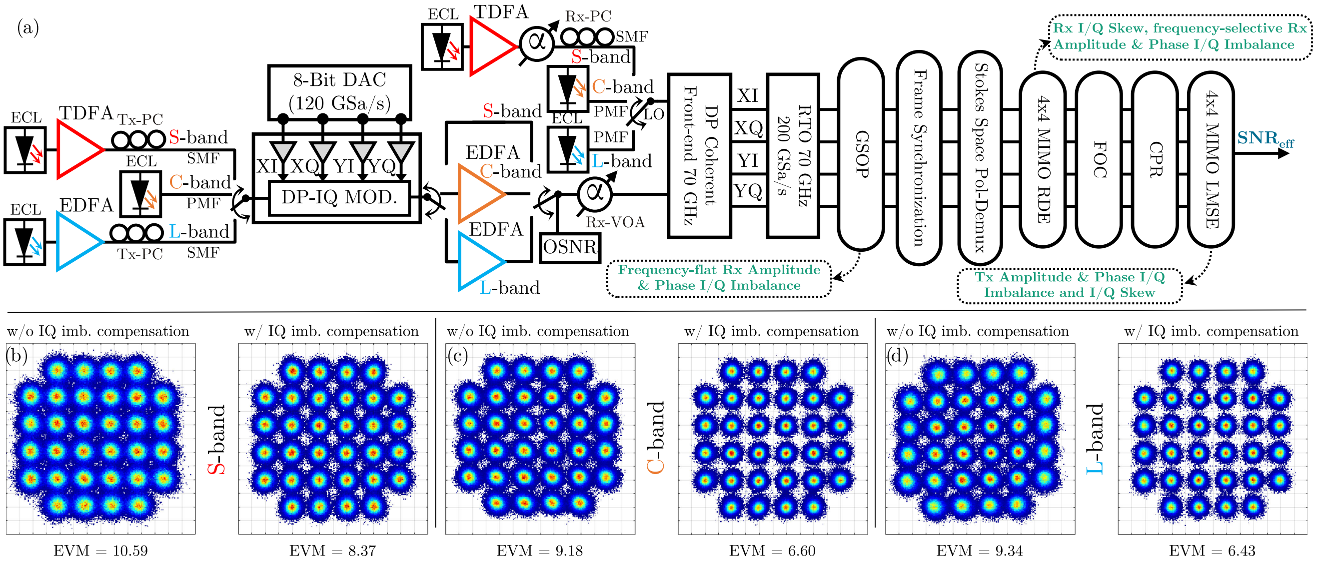

Fig. 3. (a): Experimental setup for MB back-to-back transmission with intradyne coherent reception and offline DSP for frequency-resolved I/Q imbalance characterization. PC: Polarization Controller. PMF: Polarization Maintaining Fiber. SMF: Single Mode Fiber. (b, c, d): Received constellations after DSP at 1470 nm (b), 1550 nm (c), and 1600 nm (d). For the left plots I/Q imbalance compensation through GSOP and 4x4 real-valued equalization was not performed.

where $\Delta\omega$ is the frequency offset (FO) between the optical carrier and the LO laser, $\delta(\cdot)$ is the Dirac delta function, and $*$ stands for the convolution operator. From (3), we can appreciate that the presence of a FO has the effect of rapidly mixing the I and Q signal components in time. This phenomenon results in isolating the imbalance introduced by the transmitter and allows to develop strategies to separate their monitoring from the receiver-side imbalance [6], [10]–[12]. Furthermore, the FO separation results in a fundamental difference in the impact of Tx-side and Rx-side imbalance on system performance: while we can immediately compensate for Rx-side imbalance, Tx-side imbalance lies under the surface until carrier recovery is accomplished, affecting the performance of the whole DSP chain.

III. EXPERIMENTAL SETUP

The experimental setup used for the back-to-back characterization of the wavelength-dependent I/Q imbalance from the DP I/Q modulator and the coherent receiver is provided in Fig. 3(a). The 64 GBd 32-QAM signals for the S-, C- and the L-band include Nyquist pulse shaping with a root-raised cosine at a roll-off of 0.1. The optical signals for all three bands are generated using a single commercially available C-band Lithium Niobate (LiNbO3) DP-I/Q modulator. In order to compensate for the unstable operating point of the modulator caused by wavelength and temperature dependencies, a commercially available automatic bias control (ABC; from ID-Photonics) was utilized.

Here, we remark that choosing an ideal modulator technology for multi-band operation is an open research topic. Various device characteristics have to be taken into account, such as: bandwidth, switching voltage, extinction coefficient, chirp, and linearity. The main advantage of LiNbO_3 over competing solutions (e.g., III-V semiconductor modulators) is its wider bandwidth, which can cover the entire telecommunication wavelength range from 1500 to 1600 nm [13]. This was also recently assessed in [14], where the authors experimentally compared the insertion loss (IL) from InP- and LiNbO_3-based modulators. The latter shows a relatively constant IL between 1460 and 1610 nm, whereas the former rapidly deteriorates for values below 1510 nm. Nevertheless, an important aspect of conventional LiNbO_3 technology is its increased footprint, which is not ideal for future integrated photonic systems. In this context, research effort is being directed towards the development of novel thin-film LiNbO_3 technology [15], which promise to reduce the device footprint without sacrificing the outlined benefits [13]. However, a detailed discussion on the pros and cons of multi-band technologies transcend the scope of this work.

For the S- and the L-band, an external cavity laser (ECL, with an output power of 0 dBm, $<$ 100 kHz linewidth) is coupled either to a thulium-doped fiber amplifier (TDFA) or an erbium-doped fiber amplifier (EDFA) to provide the same power as the C-Band laser (separate ECL at 16 dBm, $<$ 100 kHz linewidth) in front of the modulator. Since the S- and L-band needed to be amplified by non polarization maintaining doped fiber amplifiers, additional polarization controllers (PC) are added in front of the modulator to optimize the input polarization. As data source a 120 GSa/s, 8-bit, 4 channel digital to analog converter (DAC) in combination with four linear driver amplifiers (DA) is used to create the electrical drive signal in front of the DP-I/Q modulator. The generated transmitter 32-QAM 64 GBd waveforms are based on system identification (SI) as in [16], that was applied to the S-band [5] at 1500 nm. The achieved optical power in the S-band is wavelength-dependent and varies between -5.2 and -8 dBm from low to higher wavelength as described in detail in [17].

Per band amplification for the C-L-band is applied at the receiver while the S-band is not amplified at the output of the modulator due to the absence of a third TDFA. Please note, the absence of a booster amplifier after the modulator in the S-band results in a reduced channel power at the receiver

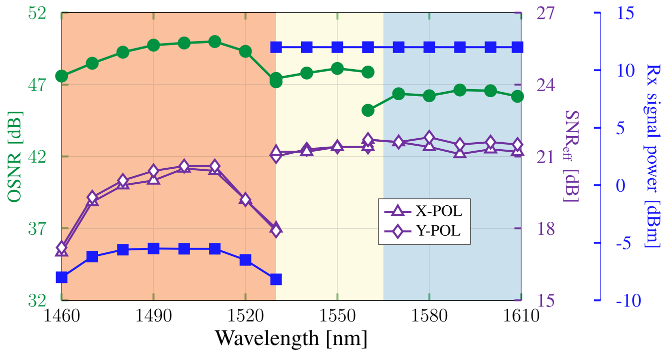

Fig. 4. OSNR (in green), effective SNR after offline DSP (in purple), and received signal power (in blue) versus wavelength for the characterized experimental setup. Each plot is referred to the axis with the same color.

and yields an unreasonable high optical signal-to-noise ratio (OSNR). The reduction of the signal input power to the Rx introduced an additional penalty in the S-band compared to the C-L-band. The OSNR for all bands is measured in front of the receiver with an optical spectrum analyzer (OSA). The resulting values as a function of wavelength are provided in Fig. 4. Selection of the band under investigation is performed using a switch before and after the modulator. The Rx signal power is reported with square symbols in Fig. 4, and the impact of its reduction in the S-band is visible in the achieved SNR in Fig. 4 for both polarizations. Here it can be seen that the measured S-band OSNR advantage compared to the C- and L-band does not translate into the achievable effective system SNR, which is lower for the S-band due to the unavailability of a third TDFA to be placed after the modulator, as done, instead, for the C- and L-band. To optimize the signal power into the coherent receiver front-end (CRF; from Fraunhofer HHI) for the C-L-band, we use a variable optical attenuator (VOA) in front of the Rx. The received signal is mixed with the local oscillator (LO) depending on the band of investigation in the 70 GHz CRF comprising an optical free-space-based C-band dual-polarization 90°-hybrid and four balanced photodetectors. A LO-laser at 14 dBm is used for the C-L-band, while for the S-band, a low-power laser is amplified up to 16 dBm and used as LO to perform intradyne coherent reception in all bands. As described for the transmitter, an additional PC is used to align the polarization after amplification in front of the LO input for the S-Band. The four electrical analog outputs of the CRF are subsequently digitized at a sampling rate of 200 GSa/s using a 4-channel real-time oscilloscope (RTO) with 70 GHz analog electrical bandwidth and 8-bit resolution.

The digitized signal is processed through data-aided DSP designed to compensate nearly ideally channel-induced impairments and provide a frequency-resolved characterization of the transceiver I/Q imbalance. After resampling at 2 samples/symbol, we apply the standard Gram-Schmidt orthonormalization procedure (GSOP) to compensate and monitor Rx-side frequency-flat amplitude and phase imbalance, as will be detailed in Section IV. The GSOP is applied over blocks of 2^{20} symbols to minimize the statistical inaccuracy of the method. The signal is then synchronized, and the two polarization tributaries are demultiplexed by signal analysis in the Stokes space [18]. At this point, we introduce a 4x4 MIMO real-valued fully-data-aided equalizer with radius-directed (RD) adaptation to compensate and monitor Rx-side I/Q skew and frequency-selective amplitude and phase imbalance. The equalizer operates in the time domain and is implemented as a finite impulse response (FIR) filter with 51 taps. This value was chosen to provide good frequency resolution for the I/Q imbalance characterization and best-case equalization performance. The output of the equalizer is downsampled to 1 sample/symbol and fed to the carrier recovery. Frequency offset compensation (FOC) is based on a periodically inserted training sequence, while the carrier phase recovery (CPR) is implemented as a moving average filter with maximum-likelihood fully-data-aided phase estimation over a window of 32 symbols. In the last step, a 4x4 real-valued MIMO post-equalizer based on fully-data-aided least mean square (LMS) adaptation is used to monitor Tx-side I/Q imbalance. A long filter of 101 taps is used to optimize equalization performance for its ability to mitigate impairments given by electrical cables and interconnects in the transmitter setup, which present a longer impulse response.

Finally, a set of received constellations at 1470, 1550 and 1600 nm are provided in Fig. 3(b)–(d). The left plots for each wavelength are obtained without (w/o) the I/Q imbalance (imba.) compensation algorithms to qualitatively show the impact of transceiver imperfections in the different bands, while the right plots are created with (w/) the discussed compensation algorithms. Additionally the error vector magnitude (EVM, given in percent and averaged over all symbols) for each wavelength w/o and with w/ imbalance compensation are normalized to peak constellation power and provided underneath the corresponding plots to quantify the transceiver imperfections.

IV. I/Q IMBALANCE CHARACTERIZATION

Inside the signal bandwidth, I/Q imbalance can in general be described as the superposition of a frequency-flat (FF), and a frequency-selective (FS) component [19]. The latter is particularly important in high symbol rate systems, where it can lead to evident system performance limitations [20]. In the following, we will use $\overline{\gamma}$, $\overline{\Phi}$ and $\overline{\Delta\tau}$ to refer to the FF components.

A. *I/Q Imbalance Estimation Principles*

As anticipated in Section II-B, we can separately monitor transmitter and receiver imbalance in the presence of FO through Rx-side DSP. In our setup, as from Fig 3, receiver imbalance is estimated through the GSOP and the 4x4 MIMO RDE.

The GSOP statistically characterizes a block of time-domain samples to provide an estimate of the FF amplitude imbalance as:

$$\overline{\gamma}_{rx} = 20\log_{10}\left(\frac{\sqrt{\langle Q_{rx}^2(t)\rangle}}{\sqrt{\langle I_{rx}^2(t)\rangle}}\right) \text{ [dB]}, \qquad (4)$$

while for the phase imbalance we have:

$$\overline{\Phi}_{rx} = \arcsin\left(\langle I_{rx}(t)Q_{rx}(t)\rangle\right). \qquad (5)$$

The estimator was proven to be accurate in back-to-back as well as after transmission [21], if $\Delta\omega\Delta\tau_{rx}$ is not large [6]. In our experiment, we monitored and measured sufficiently small values of this quantity at all wavelengths to preserve the accuracy of the monitor [4].

We can estimate the Rx-side skew and extract information about the FS amplitude and phase imbalance through the 4x4 post-equalizer. If the signal is demultiplexed into its orthogonal polarization states by the Stokes space algorithm, the operation of the 4x4 equalizer can be reduced to two separate 2x2 single-polarization matrices. In this case, we can write for each polarization:

$$\begin{bmatrix} I_{out}(t) \\ Q_{out}(t) \end{bmatrix} = \begin{bmatrix} h_{II} & h_{IQ} \\ h_{QI} & h_{QQ} \end{bmatrix} \begin{bmatrix} I_{in}(t) \\ Q_{in}(t) \end{bmatrix}. \tag{6}$$

If the signal quality at this stage is sufficiently good, the discrete Fourier transform of the time-domain equalizer taps ($H_{JK}(f) = \text{DFT}[h_{JK}(t)],\ j = \{I, Q\},\ k = \{I, Q\}$) will tend to the inverse of the frequency-domain transmission matrix. We can then monitor the frequency-resolved I/Q imbalance from the converged filter taps. In this regard, we have to remark that the uncompensated transmitter imbalance impairs the signal quality at this stage. These considerations will be taken into account when presenting the results of the characterization, as this phenomenon may have an impact on the accuracy of the receiver imbalance monitor [6].

We can repeat the same operations in the 4x4 real-valued post-equalizer employed after carrier recovery to monitor transmitter imbalance. Moreover, the requirements on sufficiently large SNR and polarization orthogonality are relaxed at this more advanced stage of the DSP chain. In this way, we estimate the transceiver amplitude imbalance as:

$$\hat{\gamma}_{tx/rx}(f) = 20\log_{10}\sqrt{\frac{|H_{II}(f)|^2 + |H_{QI}(f)|^2}{|H_{IQ}(f)|^2 + |H_{QQ}(f)|^2}}\ \ [\text{dB}], \tag{7}$$

while the phase imbalance can be monitored as

$$\hat{\Phi}_{tx/rx}(f) = \Re\left[\arctan\left(\frac{H_{II}(f)H_{QI}(f) + H_{IQ}(f)H_{QQ}(f)}{H_{II}(f)H_{QQ}(f) + H_{IQ}(f)H_{QI}(f)}\right)\right]. \tag{8}$$

At the same time, the skew can be obtained as [22]:

$$\widehat{\Delta\tau}_{tx/rx}(f) = \frac{1}{f_s}\left[\Re\left[\frac{H_{II,r}(f)}{H_{II}(f)}\right] - \Re\left[\frac{H_{QQ,r}(f)}{H_{QQ}(f)}\right]\right], \tag{9}$$

where f_s is the signal sampling frequency at the equalizer and $H_{II/QQ,r}$ is defined as the discrete Fourier transform of the time-domain filter taps vector multiplied element-wise by a discrete ramp function: $H_{II/QQ,r} = \text{DFT}(H_{II/QQ} \odot [0, 1, \ldots, N-1])$, with N being the number of taps of the equalizer.

The different impairments can be estimated from DC to the signal half Nyquist frequency. We perform our analysis up to $f \approx 30$ GHz, since moving closer to the edge of the signal bandwidth the estimation based on equalizer taps convergence rapidly loses accuracy. Finally, it is necessary to remark that, due to the presence of the GSOP, the monitored Rx-side amplitude and phase imbalance represent only the FS component. In the considered case of accurate Rx-side FF imbalance monitoring, we have:

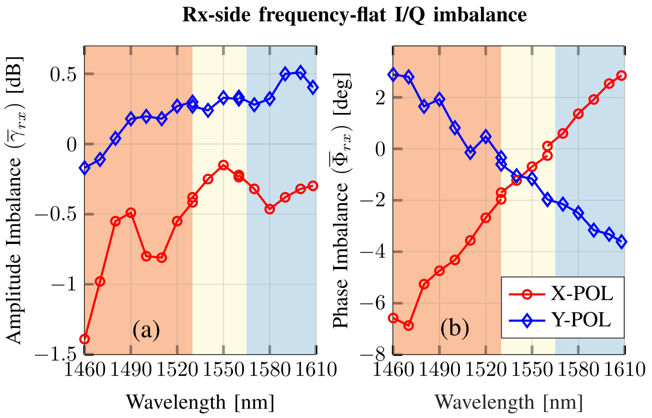

Fig. 5. Receiver FF I/Q amplitude (a) and phase (b) imbalance characterization.

$$\begin{aligned} \hat{\gamma}_{tx}(f) &\approx \gamma_{tx}(f), \\ \hat{\Phi}_{tx}(f) &\approx \Phi_{tx}(f), \\ \hat{\gamma}_{rx}(f) &\approx \gamma_{rx}(f) - \overline{\gamma}_{rx}, \\ \hat{\Phi}_{rx}(f) &\approx \Phi_{rx}(f) - \overline{\Phi}_{rx}. \end{aligned} \tag{10}$$

B. Receiver Characterization

At the beginning of the DSP chain, we characterize the FF I/Q amplitude and phase imbalance through the GSOP. While performing this operation, we monitor the quantity $\Delta\omega\Delta\tau_{rx}$ at each wavelength. As we have shown in [4], the small values observed result in an excellent accuracy of the method in this setup. In Fig. 5, we can find the results of this analysis. The FF receiver imbalance shows a clear wavelength-dependency, as noticeable from Fig. 5. This behavior originates from the imperfect operation of the receiver's optical front-end outside the C-band. Looking at the amplitude imbalance in Fig. 5(a), we observe that $\overline{\gamma}_{rx}$ varies evidently but differently for the two polarizations. These results suggest that the enhancement of $\overline{\gamma}_{rx}$ outside C-band is strongly dependent on device fabrication imperfections. For the worst-performing X-polarization, we have a maximum absolute value in C-band for $\overline{\gamma}_{rx}$ of ≈ 0.4 dB, with best-case performance at the design and calibration wavelength of 1550 nm. However, this grows up to ≈ 1.4 dB at 1460 nm. Moving to Fig. 5(b), we can similarly analyze the phase imbalance. Here we observe that in the C-band the receiver guarantees for both polarizations $|\overline{\Phi}_{rx}| < 2^\circ$, while the values grow up to $\approx 7^\circ$ in S-band. Interestingly, $\overline{\Phi}_{rx}$ shows a linear trend for both polarizations, although with inverted slopes. This behavior suggests that the imbalance is dominated by the specific design of the phase shifters inside the optical dual-polarization 90°-hybrid, with existing solutions showing a linear wavelength-dependency indeed for the phase shift introduced [9].

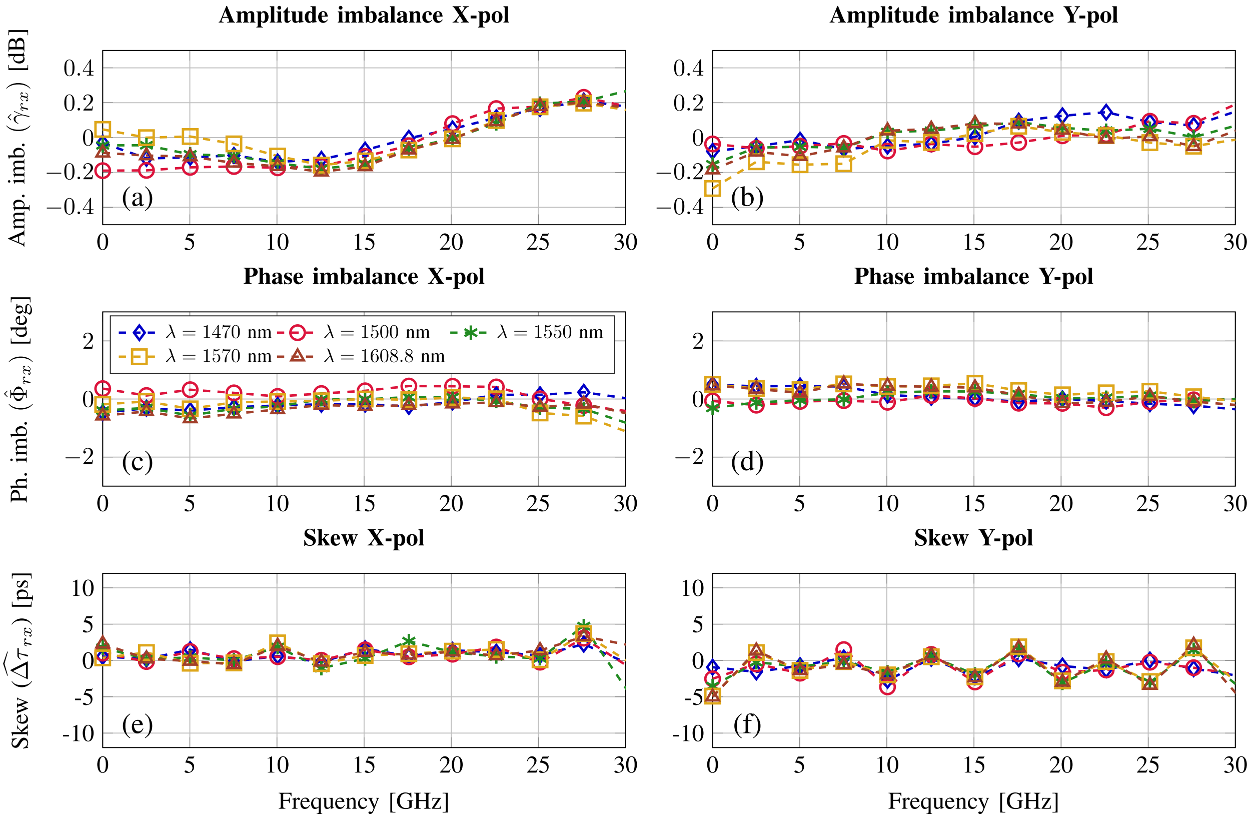

Fig. 6. Receiver FS I/Q amplitude (a), (b), phase (c), (d) imbalance, and skew (e), (f) characterization.

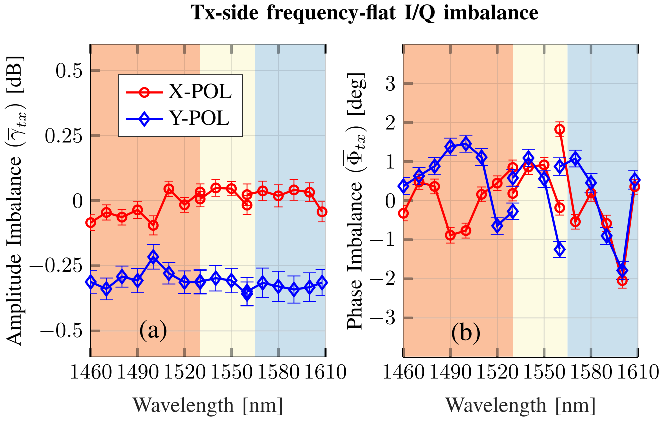

Fig. 7. Transmitter FF I/Q amplitude (a) and phase (b) imbalance characterization.

Although $\overline{\gamma}_{rx}$ and $\overline{\Phi}_{rx}$ can be severely enhanced for S-band operation, FF imbalance can be effectively counteracted by the GSOP, leading to a negligible impact on the system performance [4]. On the contrary, the GSOP does not compensate for I/Q skew and FS imbalance, which can only be mitigated by (i) more complex frequency-resolved calibration procedures and (ii) adaptive equalizers operating separately on the I and Q signal components. Both options come at a cost in MB systems. The complete calibration over the wavelength range needs considerably more characterization effort, while the equalizer requires additional complexity compared to the standard 2x2 MIMO structure used for polarization demultiplexing and channel equalization. Because of these considerations, we are interested in characterizing the FS I/Q imbalance versus the transmission wavelength. If the optical components' wavelength-dependent operation contributes only through additive FF imbalance, simple GSOP can prevent performance deterioration also for uncompensated operation outside the C-band.

In Fig. 6, we show the results of the characterization of the Rx-side FS imbalance and the I/Q skew across the S-C-L-band at $1470, 1500, 1550, 1570, 1608.8$ nm. All the data points shown are obtained as the moving average of 3 consecutive values. This operation is performed to reduce the impact of random noise on the equalizer's taps convergence. From Fig. 6(a)–(d) we can immediately notice that the FS amplitude and phase imbalance takes very similar values for all wavelengths. This is a major result of this work since it demonstrates that the wavelength-dependency of the receiver imbalance impacts only the FF component. This behavior is a consequence of the linearity of the optical 90°-hybrid and photo detector's response over the signal bandwidth versus wavelength. Another remark is given by the small values assumed by the imbalance for both polarizations: $|\hat{\gamma}_{rx}| < 0.4$ dB, $|\hat{\Phi}_{rx}| < 0.4°$. This indicates (i) that the previously performed GSOP has effectively mitigated the wavelength-dependent FF imbalance and (ii) that the performed frequency-resolved calibration effectively removed the FS imbalance arising from the electrical front-end.

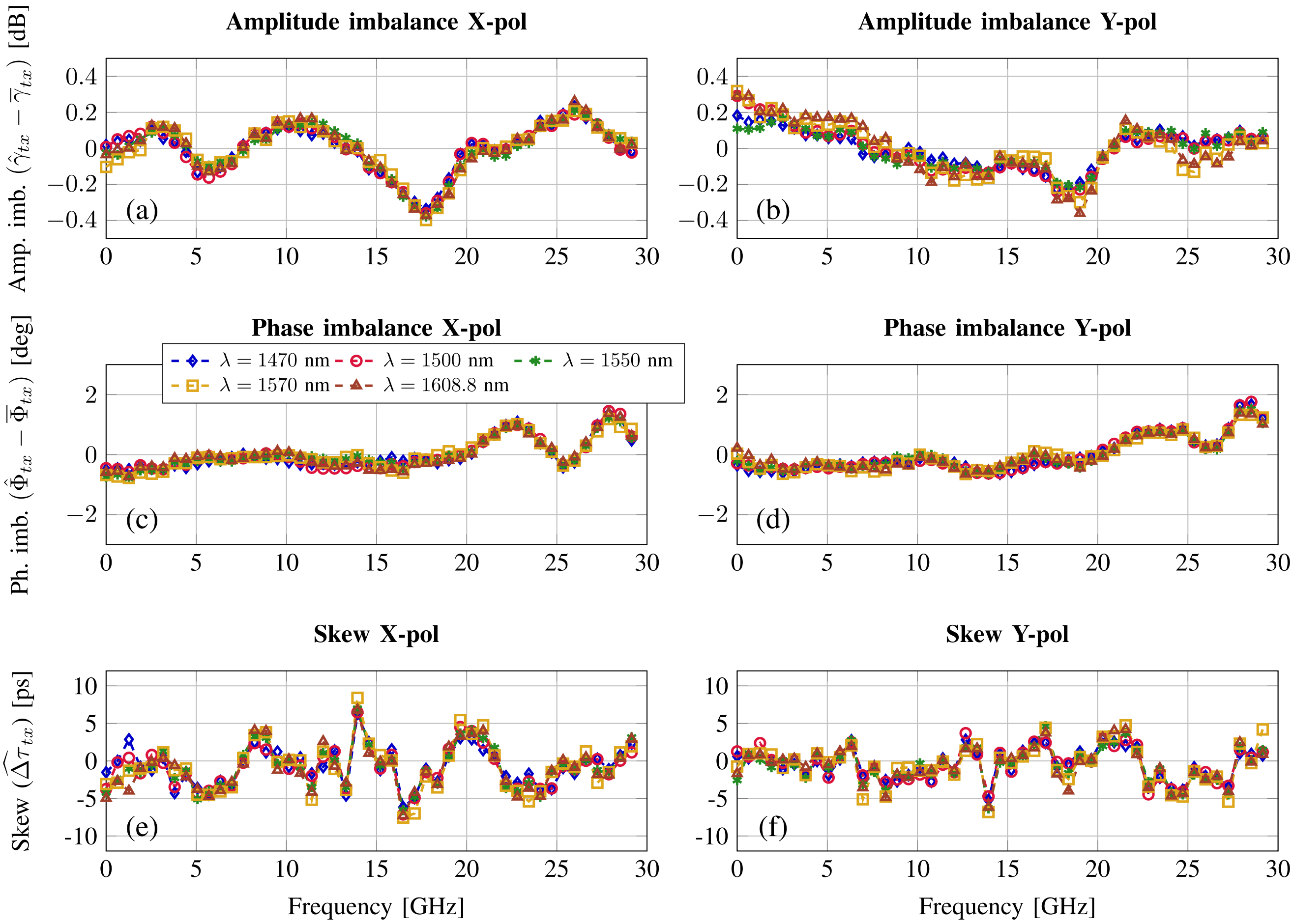

Fig. 8. Transmitter FS I/Q amplitude (a),(b), phase (c),(d) imbalance, and skew (e),(f) characterization.

In Fig. 6(e)–(f), the monitored receiver skew is plotted for each analyzed wavelength. Skew is generated in the electrical components and is thus not expected to be wavelength-dependent. However, we monitor its value for all measurements for validation purposes. As we can see, the receiver skew assumes minimal values. Averaging over the analyzed frequency range we have for the X- and Y-polarization, respectively, $\overline{\Delta\tau}_{rx,X} \approx 0.25$ ps and $\overline{\Delta\tau}_{rx,Y} \approx -0.31$ ps. Finally, the absence of any evident skew is another clear indicator of the effectiveness of the performed receiver calibration.

C. Transmitter Characterization

As detailed in Section IV-A, we can monitor transmitter impairments after carrier recovery from the converged taps of the 4x4 MIMO post-equalizer. As already done for the Rx-side analysis, we start by investigating FF amplitude and phase imbalance. These can be obtained by averaging the estimated $\hat{\gamma}_{tx}(f)$ and $\hat{\Phi}_{tx}(f)$. The resulting values versus wavelength are reported in Fig. 7, together with the relative 95% confidence intervals for the calculated mean values. According to the central limit theorem, these are obtained as the standard error of the mean scaled by a factor 1.96.

The FF amplitude imbalance, in Fig. 7(a), shows a very flat behavior versus wavelength and small estimated values $|\overline{\gamma}_{tx}| <$ 0.35 dB. The monitored FF phase imbalance, reported in Fig. 7(b), also does not show any clear wavelength-dependency. However, its values show a larger variability than for the amplitude imbalance. We can explain these fluctuations by considering the operation of the 90° phase shifter in the modulator. It is well known that bias drift is a drawback of optical modulators based on $\mathrm{LiNbO_3}$ technology [23], and it results in small phase mismatch fluctuations in time, also in the presence of an ABC. This behavior can be easily noticed by looking at 1530 nm and 1560 nm, where two sets of data obtained with different lasers and amplification schemes are available: While we observe that the confidence intervals of the two measurements overlap for the amplitude imbalance, this is not the case for the phase imbalance because of the bias drift. Finally, for our experimental results, we can confirm that there was no noticeable difference in the temporal dynamic of the bias drift in the presence of an active ABC over the whole investigated wavelength range.

The absence of wavelength-dependency in the transmitter FF imbalance strongly differentiates from what we observed on the receiver side, where the optical components have been found responsible for substantial FF imbalance variations over the analyzed wavelength range. This behavior indicates: (i) the lack of evident degradation in the power splitting and combining operations and (ii) the effectiveness of standard automated bias control to adapt the modulator operation in a multi-band scenario. In particular, the estimated imbalance values and their confidence intervals remain small over the whole wavelength range, proving the absence of wavelength-dependency in the behavior of the estimator.

We analyze at this point FS Tx-side imbalance similarly as we did previously for the receiver. However, in this case, the GSOP does not compensate for the FF component of the transmitter imbalance, so the 4x4 post-equalizer directly monitors the combination of FF and FS amplitude and phase imbalance. We obtain the FS imbalance by subtraction from the total estimated value of the FF component and show its characterization in Fig. 8, where the data points are obtained as the moving average of 5 consecutive values. For all transmitter imperfections, we observe negligible variations in the spectrum of the imbalance for the different wavelengths considered. As already discussed when analyzing the receiver in Section IV-B, this behavior proves the linearity of the operation of the optical components versus wavelength, resulting in a wavelength-dependency that is exclusive to the FF imbalance component. These results, together with the ones in Fig. 7, are crucial to assess the impact of the wavelength-dependency of I/Q imbalance on the performance of MB systems as well as the complexity requirements for their effective monitoring and compensation. It is critical to compensate and monitor transmitter imbalance since they impair the operation of the whole DSP chain [4], contrary to what has been discussed for Rx-side impairments. On the transmitter side, FS imbalance variations could be compensated only by additional adaptation of the DPD per wavelength. In contrast, the minor FF imbalance variations observed can be corrected through more simple automatic control strategies based on power monitoring. Moreover, on the receiver side, a single-tap post-equalizer can effectively mitigate and monitor residual FF imbalance. On the contrary, FS variations could only be compensated through longer adaptive filters, leading to more significant power consumption and system complexity.

Additionally, we notice that the FS amplitude and phase impairments in Fig. 8(a)–(d) have a more prominent frequency-dependent behavior over the signal bandwidth compared to the equivalent receiver imbalance. For both signal polarization states, the FS amplitude imbalance in Fig. 8(a)–(b) has a peak at around 18 GHz. Moreover, we observe also a slightly larger imbalance in the lower frequency range in the Y-polarization. However, all the values are contained in a remarkably small range ± 0.4 dB, validating the effectiveness of the DPD performed. Similar considerations can be made for the characterized FS phase imbalance in Fig. 8(c)–(d), for which fluctuations up to $\approx 2^\circ$ are observed for frequency above 20 GHz. These values, although small, are also larger than the ones observed for the receiver imbalance, where the frequency-resolved calibration mitigated FS phase imbalance almost perfectly. Their wavelength-independence allows, however, for a one-time additional calibration and compensation if extremely high-order modulation formats are employed [20], [24]. In Fig. 8(e)–(f) the monitored transmitter skew is shown. For the X- and Y-polarization we characterize $\overline{\Delta\tau}_{tx,X} = -0.7$ ps and $\overline{\Delta\tau}_{tx,Y} = -0.43$ ps, respectively. Also in this case, the values are higher than for the receiver and present larger variability, but do not present any critical behavior.

As a final remark, the small monitored imbalance further supports the outcome of the Rx-side imbalance characterization. As previously discussed, in the presence of significant transmitter impairments, the monitoring accuracy for the receiver imbalance would be degraded by a large effective reduction in the signal quality before carrier recovery, and post-equalization [6].

V. CONCLUSION

In this work, we reported about the characterization of the frequency-resolved I/Q imbalance versus the wavelength of operation in off-the-shelf C-band transceivers operating in the S-C-L-band. We have shown that the overall wavelength-dependency of I/Q amplitude and phase imbalance is strong for the considered coherent receiver due to the significant sensitivity of the 90°-hybrid to the wavelength of operation. However, the variability of these impairments inside the signal bandwidth presented exclusively a frequency-flat component, which can be efficiently and effectively monitored and compensated by standard digital compensation methods as the GSOP. On the contrary, the characterized $LiNbO_3$ modulator did not show any clear wavelength-dependency for the frequency-flat imbalance or its frequency-selective component for all the tested wavelengths inside the signal bandwidth. These findings prove the interoperability of commercial transceivers optimized and calibrated for C-band operation in multi-band networks, even without the imperative need for costly wavelength-dependent calibration, DPD procedures, and higher receiver-side DSP complexity.

REFERENCES

[1] A. Ferrari *et al.*, "Assessment on the achievable throughput of multi-band ITU-T G. 652. D fiber transmission systems," *J. Lightw. Technol.*, vol. 38, no. 16, pp. 4279–4291, Aug. 2020.

[2] H. Sun *et al.*, "800G DSP ASIC design using probabilistic shaping and digital sub-carrier multiplexing," *J. Lightw. Technol.*, vol. 38, no. 17, pp. 4744–4756, 2020.

[3] L. Galdino *et al.*, "Optical fibre capacity optimisation via continuous bandwidth amplification and geometric shaping," *IEEE Photon. Technol. Lett.*, vol. 32, no. 17, pp. 1021–1024, Sep. 2020.

[4] G. Di Rosa, R. Emmerich, M. Sena, J. K. Fischer, C. Schubert, and A. Richter, "Impact of wavelength-dependent I/Q imbalances of standard c-band transceivers in rate-adaptive multiband systems," in *Proc. Eur. Conf. Opt. Commun.*, 2021, pp. 1–4.

[5] R. Emmerich *et al.*, "Enabling S-C-L-band systems with standard C-band modulator and coherent receiver using nonlinear predistortion," in *Proc. Opt. Fiber Conf.*, 2021, pp. 1–3, Paper F4D.7.

[6] J. Liang, Y. Fan, Z. Tao, X. Su, and H. Nakashima, "Transceiver imbalances compensation and monitoring by receiver DSP," *J. Lightw. Technol.*, vol. 39, no. 17, pp. 5397–5404, Sep. 2021.

[7] M. Sena *et al.*, "Performance evaluation of InP-based DP-IQ modulators for multiband transmission systems," in *Proc. 22nd Int. Conf. Transp. Opt. Netw.*, 2020, pp. 1–4.

[8] M. Sena *et al.*, "Bayesian optimization for nonlinear system identification and pre-distortion in cognitive transmitters," *J. Lightw. Technol.*, vol. 39, no. 15, pp. 5008–5020, 2021.

[9] Y. Nasu, T. Mizuno, R. Kasahara, and T. Saida, "Temperature insensitive and ultra wideband silica-based dual polarization optical hybrid for coherent receiver with highly symmetrical interferometer design," *Opt. Exp.*, vol. 19, no. 26, pp. B112–B118, 2011.

[10] Q. Zhang, Y. Yang, C. Gu, Y. Yao, A. P. T. Lau, and C. Lu, "Multi-dimensional, wide-range, and modulation-format-transparent transceiver imbalance monitoring," *J. Lightw. Technol.*, vol. 39, no. 7, pp. 2033–2045, Apr. 2020.

[11] Q. Zhang *et al.*, "Algorithms for blind separation and estimation of transmitter and receiver IQ imbalances," *J. Lightw. Technol.*, vol. 37, no. 10, pp. 2201–2208, May 2019.

[12] C. Ju, N. Liu, and C. Li, "In-service blind transceiver IQ imbalance and skew monitoring in long-haul non-dispersion managed coherent optical systems," *IEEE Access*, vol. 7, pp. 150051–150059, 2019.

[13] V. M. Petrov, P. M. Agruzov, V. V. Lebedev, I. V. Il'ichev, and A. V. Shamray, "Broadband integrated optical modulators: Achievements and prospects," *Phys.-Uspekhi*, vol. 64, no. 7, pp. 722–739, 2021.

[14] R. Emmerich *et al.*, "Enabling S-C-L-band systems with standard C-band modulator and coherent receiver using coherent system identification and nonlinear predistortion," *J. Lightw. Technol.*, vol. 40, no. 5, pp. 1360–1368, Mar. 1, 2022.

[15] A. Rao *et al.*, "High-performance and linear thin-film lithium niobate Mach-Zehnder modulators on silicon up to 50GHz," *Opt. Lett.*, vol. 41, no. 24, pp. 5700–5703, Dec. 2016. [Online]. Available: http://www.osapublishing.org/ol/abstract.cfm?URI=ol-41-24-5700

[16] M. Nölle, M. S. Erkilinç, R. Emmerich, C. Schmidt-Langhorst, R. Elschner, and C. Schubert, "Characterization and linearization of high bandwidth integrated optical transmitter modules," in *Proc. Eur. Conf. Opt. Commun.*, 2020, pp. 1–4, Paper Tu2D-4.

[17] R. Emmerich *et al.*, "S-band transmission with off-the-shelf C-band components enabled by nonlinear predistortion based on coherent system identification," in *Proc. IEEE Photon. Netw., 22th ITG Symp.*, 2021, pp. 77–83.

[18] B. Szafraniec, B. Nebendahl, and T. Marshall, "Polarization demultiplexing in Stokes space," *Opt. Exp.*, vol. 18, no. 17, pp. 17928–17939, 2010.

[19] A. Mohammadian and C. Tellambura, "RF impairments in wireless transceivers: Phase noise, CFO, and IQ imbalance - A survey," *IEEE Access*, vol. 9, pp. 111718–111791, 2021.

[20] X. Chen and D. Che, "Direct-detection based frequency-resolved I/Q imbalance calibration for coherent optical transmitters," in *Proc. Opt. Fiber Commun. Conf. Exhibit.*, 2021, pp. 1–3.

[21] Y. Fan, Y. Jiang, J. Liang, Z. Tao, H. Nakashima, and T. Hoshida, "Transceiver IQ imperfection monitor by digital signal processing in coherent receiver," in *Proc. 24th OptoElectron. Commun. Conf. Int. Conf. Photon. Switching Comput.*, 2019, pp. 1–3.

[22] C. R. S. Fludger and T. Kupfer, "Transmitter impairment mitigation and monitoring for high baud-rate, high order modulation systems," in *Proc. 42nd Eur. Conf. Opt. Commun.*, 2016, pp. 1–3.

[23] J. P. Salvestrini, L. Guilbert, M. Fontana, M. Abarkan, and S. Gille, "Analysis and control of the DC drift in $LiNbO_3$-based Mach–Zehnder modulators," *J. Lightw. Technol.*, vol. 29, no. 10, pp. 1522–1534, May 2011.

[24] Y. Yoshida, S. Yoshida, S. Oda, T. Hoshida, and N. Yamamoto, "Simultaneous monitoring of frequency-dependent IQ imbalances in a dual-polarization IQ modulator by using a single photodetector: A phase retrieval approach," in *Proc. Opt. Fiber Commun. Conf. Exhibit.*, 2021, pp. 1–3.

Gabriele Di Rosa (Graduate Student Member, IEEE) received the B.Sc. degree (*cum laude*) in electronic engineering from Politecnico di Torino, Turin, Italy, in 2016, and the double M.Sc. degree (*cum laude*) in electronic engineering from Politecnico di Torino, and in electrical engineering from the KTH Royal Institute of Technology, Stockholm, Sweden, in 2019. He is currently working toward the Ph.D. degree with the Technical University of Berlin, Berlin, Germany. He is also with VPIphotonics GmbH, Berlin, Germany, as an early-stage Researcher of the Marie Skłodowska-Curie European Training Network WON. While pursuing the M.Sc. degree in 2019, he was a Product Development Engineer with Finisar AB, Järfälla, Sweden. His research interests include ultra-wideband fiber-optic coherent communications, digital signal processing, advanced modulation techniques, and transceiver optimization.

Robert Emmerich was born in Meiningen, Germany, in 1982. He received the B. Eng. degree in telecommunication engineering from the University of Applied Sciences HTW-Berlin, Berlin, Germany, in 2013, and the M.Sc. degree in electrical engineering from the Technische Universität Berlin, Berlin, Germany, in 2015. He is currently working toward the Ph.D degree with the Fraunhofer Institute for Telecommunications, Heinrich-Hertz-Institute, Berlin, Germany. Since 2016, he has been a Research Associate with the Fraunhofer Institute for Telecommunications. His research interests include application of multiband transmission systems with higher order modulation and broadband digital coherent receivers and transmitters.

Matheus Sena (Graduate Student Member, IEEE) received the B.Sc. and M.Sc. degrees in electrical engineering from the Federal University of Pernambuco, Recife, Brazil, in 2016 and 2018, respectively. In 2014, he was with the Polytechnic School of Engineering, New York University, New York, NY, USA. He is currently working toward the Ph.D. degree with the Technische Universität Berlin, Berlin, Germany. Since 2019, he has been a Research Associate with the Fraunhofer Institute for Telecommunications, Heinrich-Hertz-Institute, Berlin, Germany. His research interests include cognitive transponders, precompensation techniques, multiband transmission systems, and application of machine learning algorithms in optical communications.

Johannes K. Fischer (Senior Member, IEEE) received the Dipl.-Ing. and Dr.-Ing. degrees in electrical engineering from the Technische Universität Berlin, Berlin, Germany, in 2003 and 2009, respectively. In 2010, he joined the Fraunhofer Institute for Telecommunications, Heinrich Hertz Institute, Berlin, Germany, where he is currently heading a research group on digital signal processing with the Department of Photonic Networks and Systems. He is the author or coauthor of more than 120 articles and a book chapter. His research interests include advanced modulation formats, digital signal processing, and machine learning for optical systems. Dr. Fischer is a Member of the VDE, where he is with working Group KT 3.1 "Modelling of Photonic Components and Systems" of the Information Technology Society. He was with the Technical Program Committees of OECC and OFC.

Colja Schubert received the Dipl.-Phys. and Dr. rer. nat. degrees in physics from Technische Universität Berlin, Berlin, Germany, in 1998 and 2004, respectively. From 1996 to 1997, he was a Exchange Student with Strathclyde University, Glasgow, U.K. During his Dipl. thesis from 1997 to 1998, he was with Max-Born-Institute for Nonlinear Optics and Short Pulse Spectroscopy, Berlin, Germany. Since 2000, he has been a Member of the scientific staff with Heinrich-Hertz-Institute, Berlin, Germany. His research interests include high-speed transmission systems and all-optical signal processing. He is currently heading the Submarine and Core Systems Group with Department of the Photonic Networks and Systems. Dr. Schubert is a Member of the German Physical Society.

Ronald Freund received the Dipl.-Ing. and Dr.-Ing. degrees in electrical engineering from the Technical University of Ilmenau, Ilmenau, Germany, in 1993 and 2002, respectively, and the M.B.A. degree from RWTH Aachen University, Aachen, Germany. In 1997, he co-founded VPI Systems Inc., where he was involved in as the Chief Technology Officer and a Consultant, responsible for the development of design software for the physical layer of photonic networks. Since 1995, he has been with Heinrich Hertz Institute, Berlin, Germany, where he is currently leading the Department of Photonic Networks and Systems. In 2017, he has been appointed as a Professor of photonic communication systems with the Technical University of Berlin, Berlin, Germany. He has authored or coauthored more than 150 scientific publications.

André Richter (Senior Member, IEEE) received the M.Sc. degree in electrical engineering from the Georgia Institute of Technology, Atlanta, GA, USA, in 1995, and the Dipl.-Ing. and Dr.-Ing. degrees from the Technical University of Berlin, Berlin, Germany, in 1997 and 2002, respectively, for novel work in modeling long haul fiber optical communications. In 1998, he was a Research Fellow with the University of Maryland Baltimore County, Baltimore, MD, USA. Since 1997, he has been with the VPIphotonics Team, Berlin, Germany. He has coauthored more than 120 publications, including two book chapters. His research interests include modeling and design aspects of optical communications, fiber-optics, and integrated photonics, and in developing professional software solutions addressing these fields. He invoked an industry training program that served more than 1000 engineers and contributed to many co-funded research programs. He led international teams in application engineering, product management, research and development before being appointed as a General Manager in 2013. He is a Senior Member of OSA, and Member of VDE/ITG and SPIE. He was with several technical program committees of OFC, ACP, and Summer Topicals.